Original Article

Three-dimensional simulations of resistance spot welding

Chris V Nielsen[1], Wenqi Zhang[2], William Perret[3], Paulo AF Martins[4] and Niels Bay[1]

Abstract

This paper draws from the fundamentals of electro-thermo-mechanical coupling to the main aspects of finite element implementation and three-dimensional modelling of resistance welding. A new simulation environment is proposed in order to perform three-dimensional simulations and optimization of resistance welding together with the simulations of conventional and special-purpose quasi-static mechanical tests. Three-dimensional simulations of resistance welding consider the electrical, thermal, mechanical and metallurgical characteristics of the material as well as the operating conditions of the welding machines. Simulations of the mechanical tests take into account material softening due to the accumulation of ductile damage and cover conventional tests, such as tensile–shear tests, cross-tension test and peel tests, as well as the possibility of special-purpose tests designed by the users. The overall presentation is supported by numerical simulations of electrode misalignment caused by the flexibility of the welding machine arms and electrical shunting due to consecutive welds in the resistance spot welding of two sheets.

Introduction

Resistance spot welding is the most preferred and widely used technology for joining different types and combinations of sheet metal parts in automotive body-in-white assemblies. An average midsized passenger car contains several thousand spot welds which ensure the rigidity and the strength of the overall assembly but also introduce difficulties in the project, design and fabrication methods.

The major difficulties in resistance spot welding are caused by variations in the material properties and combinations, the surface conditions and the electrode wear. The challenges to the welding engineer are to design process operating parameters such as the current, the time, the force and the choice of electrode type in order to gain a weld schedule that meets the quality requirements of the weld, while being robust towards changing conditions, e.g. in alignment or in surface conditions.

Numerical simulations can assist experimental work by providing a detailed understanding of the process and being a framework for trying different parameters, geometries and set-ups for guiding the experimental work. In 1961, Greenwood[1] introduced the first axisymmetric heat conduction model based on the finite difference method and, in 1984, Nied[2] introduced the first non-linear axisymmetric electro-thermo-mechanical finite element model for resistance spot welding, which was a large step forwards. However, because the model was based on small-strain formulations, like many others that were developed in the 1980s,[3] it is nowadays seen as inadequate for replicating the contact and material behaviour during the formation and growth of the weld nuggets.

The research work performed in the 1990s and 2000s was focused on the contact models, the formation and

[1]Department of Mechanical Engineering, Technical University of Denmark, Kongens Lyngby, Denmark
[2]SWANTEC Software and Engineering ApS, Kongens Lyngby, Denmark
[3]Audi AG, Joining Technology Development, Ingolstadt, Germany
[4]Instituto Superior Tecnico, Universidade de Lisboa, Lisboa, Portugal

Corresponding author:
Chris V Nielsen, Department of Mechanical Engineering, Technical University of Denmark, Produktionstorvet 425, DK-2800 Kongens Lyngby, Denmark.
Email: cvni@mek.dtu.dk

growth of nuggets and the occurrence of expulsion in resistance spot welding. Developments in large-strain formulations in conjunction with progress in computing technology allowed improvement and consolidation of electro-thermo-mechanical finite element models for resistance spot welding. The investigations performed in this period were mainly based on existing commercial software. Tsai et al.,[4] for example, utilized the commercial finite element program ANSYS to analyse the influences of various operative parameters in resistance spot welding, and Khan et al.[5] employed a coupled electro-thermo-mechanical model based on the commercial finite element program ABAQUS to predict the formation and growth of nuggets. The developments in this period also gave rise to the development of special-purpose computer programs whicht extended the range of potential users to professional welding engineers not working at universities or research institutes. Zhang et al.[6] presented the first electro-thermo-mechanical finite element computer program specifically developed for resistance welding that subsequently evolved into the commercial program SORPAS, which is nowadays a reference in the automotive industry worldwide.

The majority of the numerical developments in resistance spot welding that were performed in the 1990s and 2000s were carried out with two-dimensional axisymmetric or simple three-dimensional finite element models. Huh and Kang,[7] for example, developed the first three-dimensional finite element computer program for resistance spot welding taking the temperature-dependent electrical and thermal properties of the materials into account but omitting the plastic deformation of the materials. Other researchers such as Feulvarch et al.[8] proposed general three-dimensional finite element formulations of the electro-thermal conditions at the contacting surfaces but restricted their investigation to axisymmetric welding of sheets.

As a result of this, the current state of development in numerical simulations of resistance spot welding is in the need for an environment for effectively handling the technical difficulties related to the electrode misalignment and shunt effects, which are known to have significant influences on the overall quality of the welded joints as well as on the width of the acceptable process window. Moreover, this need is expected to grow in the coming years because of the additional technical difficulties and challenges that are posed by the resistance spot welding of advanced high-strength steels and new ultra-high-strength steels compared with conventional mild steels.[9, 10] Welding of aluminium alloys poses further challenges to welding engineers.

Evaluation and prediction of the weld strength are other challenges. Aslanlar et al.,[11] for example, performed experimental investigations on the influence of the welding time on the peel strength and the tensile–shear strength of resistance-spot-welded joints. More recently, Xu et al.[12] analysed the locations and onset of failure and necking in lap shear tests by analytical

stress functions and elasto-plastic finite element analysis under plane stress conditions; also, Radakovic and Tumuluru[13] performed finite element modelling of the cross-tension test and discussed its validity to represent the loading of the spot welds in a vehicle undergoing a crash event. Lin et al.[14] proposed a different methodology to obtain the relationship between the spot-welding parameters and the tensile–shear strength of test specimens by means of a Taguchi-based neural network algorithm. Finally, Ouisse and Cogan[15] presented a methodology to design and compare spot-welded automobile structures.

The aims and objectives of this paper is to present the theoretical and numerical fundamentals that provide support to the first finite element computer environment (SORPAS 3D) which is specifically designed and developed to perform three-dimensional modelling, optimization and mechanical testing of resistance welding. It is developed into an easy-to-use desktop environment to be utilized by professional engineers in industry. The presentation includes results from the numerical modelling of the electrode misalignment and shunt effects in resistance spot welding together with results from the numerical modelling of tensile–shear tests. The example of the electrode misalignment is substantiated by a corresponding experiment.

The simulations of strength testing are directly performed from the resistance-spot-welding models after unloading the electrodes and cooling in air to room temperature. This is a novel approach, compared with the traditional simulations available in the literature which include a rigid nugget or an assumed initial stress field to induce the weld properties.

The paper is organized in four sections. The following section provides an overview of the fundamentals of the electro-thermo-mechanical modelling of resistance welding. Then follows a section addressing numerical modelling topics related to the geometry and size of the testing specimens, the discretization by hexahedral finite elements, the temperature-dependent material properties and the welding conditions. The last section, before the conclusions, presents and discusses the results obtained in the numerical modelling of the electrode misalignment, the shunt effects and the subsequent tensile–shear tests.

Fundamentals of electro-thermo-mechanical modelling

The integrated resistance welding and mechanical testing simulation environment of SORPAS 3D was developed by SWANTEC Software and Engineering ApS in collaboration with the Technical University of Denmark and the University of Lisbon. The program performs the coupled electro-thermo-mechanical finite element simulation of resistance welding and the damage-coupled finite element simulations of quasi-static mechanical tests.

Mechanical module

The mechanical module allows the contact interfaces, the deformation of the welded parts and the distribution of the major field variables (e.g. the stresses and the strains) during the formation and growth of nuggets to be modelled, taking into account the temperature-dependent mechanical properties of the materials. The mechanical module is built upon the finite element flow formulation, which is based on the weak variational form

$$\int_V \bar{\sigma}\,\delta\dot{\bar{\varepsilon}}\,\mathrm{d}V + K\int_V \dot{\varepsilon}_{ii}\,\delta\dot{\varepsilon}_{jj}\,\mathrm{d}V - \int_{S_t} t_i\,\delta u_i\,dS = 0 \qquad (1)$$

where V is the domain volume limited by the surfaces S_u and S_t, where the velocities u_i and the tractions t_i are prescribed, $\bar{\sigma}$ is the effective stress and $\dot{\bar{\varepsilon}}$ is the effective plastic strain rate. The symbol K denotes a large positive number related to the mean stress $\sigma_m = \sigma_{kk}/3$ through $K\dot{\varepsilon}_{kk} = 2\sigma_m$, which is necessary to impose the incompressibility requirements $\dot{\varepsilon}_{kk} = 0$ of the plastic deformation of metallic materials.

Numerical implementation of the finite element flow formulation performed in SORPAS 3D allows plastic deformation to follow either the isotropic von Mises yield criterion

$$\bar{\sigma}^2 = 3J_2 \qquad (2)$$

where J_2 is the second invariant of the deviatoric stress tensor, or the anisotropic Hill quadratic yield criterion

$$2\bar{\sigma}^2 = F\left(\sigma_y - \sigma_z\right)^2 + G\left(\sigma_z - \sigma_x\right)^2 + H\left(\sigma_x - \sigma_y\right)^2 + 2L\tau_{yz}^2 + 2M\tau_{zx}^2 + 2N\tau_{xy}^2 \qquad (3)$$

where the constants F, G, H, L, M and N are to be determined from material testing.

In the case of quasi-static mechanical tests, it is possible to account for the accumulation of damage by means of the constitutive equations of metallic materials with the initial porosity based on the yield criteria due to Shima and Oyane[16] or Doraivelu et al.[17] and given by

$$\bar{\sigma}_R^2 = A\,J_2 + B\,I_1 \qquad (4)$$

In the above equation, I_1 is the first invariant of the stress tensor σ_{ij} and $\bar{\sigma}_R^2 = C\bar{\sigma}^2$ is the effective stress response of the material, taking into account the decrease in the relative density R due to accumulation of damage (generation and coalescence of voids). A, B and C are material constants which depend on the relative density.

The accountability of damage directly from the relative density instead of the plastic strain[13] is a step further for the numerical simulations of quasi-static mechanical tests, which deals with the modern trends in damage mechanics.[18] In fact, the main advantage of using the constitutive equations of metallic materials with an initial porosity instead of the standard von Mises or Hill constitutive equation is the possibility of directly influencing the predicted load–displacement curves of the tests by the accumulation of ductile damage in the regions of the specimens undergoing large plastic deformations. A measure of the damage D is defined as

$$D = 1 - R \qquad (5)$$

such that it is zero when the material is fully dense, and decreasing relative density corresponds to increasing damage.

Thermal module

The thermal module calculates the heat transfer and heat generation, including the temperature-dependent properties of the materials. The module accounts for the heat generated by the electrical Joule effect and plastic work and for the heat exchange with the electrodes and surrounding environment. The weak variational form of the thermal module is built upon the classical Galerkin treatment of the heat transfer equation

$$\int_V kT_{,i}\,\delta T_{,i}\,\mathrm{d}V + \int_V \rho_m c_m \dot{T}\,\delta T\,\mathrm{d}V - \int_V \dot{q}_V\,\delta T\,\mathrm{d}V$$
$$- \int_S \dot{q}_S\,\delta T\,\mathrm{d}S - \int_S kT_{,n}\,\mathrm{d}S = 0 \qquad (6)$$

In the above equation, the thermal conductivity k is related to heat conduction, the mass density ρ_m and the heat capacity c_m are related to the rate of stored energy per unit volume, giving rise to a temperature rate $\dot{T}$, and the rate of heat generation $\dot{q}_V$ in the material volume includes the contributions due to dissipated energy given by

$$\dot{q}_{plastic} = \beta\,\bar{\sigma}\dot{\bar{\varepsilon}}$$
$$\dot{q}_{electrical} = \rho j^2 \qquad (7)$$

where β is a constant taking values in the range between 0.85 and 0.95, ρ is the electrical resistivity and j is the current density. The rate $\dot{q}_S$ of heat generation along surfaces includes the contributions

$$\dot{q}_{convection} = -h\left(T_s - T_f\right)$$
$$\dot{q}_{radiation} = -\varepsilon_{emis}\sigma_{SB}\left(T_s^4 - T_f^4\right) \qquad (8)$$
$$\dot{q}_{friction} = \tau_f |v_r|$$

where h is the heat transfer coefficient, T_s is the surface temperature, T_f is the temperature of the surroundings, ε_{emis} is the emissivity coefficient, σ_{SB} is the Stefan–Boltzmann coefficient, τ_f is the friction shear stress at the contact interfaces between the parts (or sheets) to be welded and v_r is the relative sliding velocity at the

contact interfaces between the parts (or sheets) to be welded.

Electrical module

The electrical module calculates the distribution of the electric potential Φ which, after differentiation and multiplication by the conductivity, provides the current density j at all locations in the electrodes and the parts to be welded. The electrical module takes into account the temperature-dependent electrical properties of the materials, and its governing equation is built upon integration of the Laplace equation for an arbitrary variation $\delta\Phi$ in the electric potential, which by applying the divergence theorem results in

$$\int_V \Phi_{,i}\,\delta\Phi_{,i}\,\mathrm{d}V = \int_S \Phi_{,n}\,\mathrm{d}S \qquad (9)$$

where $\Phi_{,n}$ is the normal gradient of the electric potential to the free surfaces (which is zero and therefore cancels out the right-hand side).

Although this approach considers the distribution of the electric potential Φ to be solely determined by the geometry under steady-state conditions ($\dot{\Phi} = 0$), it is generally considered a good methodology because an electric field has a much faster reaction rate than a temperature field does.[19]

The current density is calculated from $j_i = \Phi_{,i}/\rho$, where the electrical resistivity ρ is temperature dependent. Its value is of special importance at the contact interfaces where the majority of the heat is generated in the early stages of welding. The contact resistivity ρ_c is modelled as[20]

$$\rho_c = \frac{3\sigma_{soft}}{\sigma_n}\left(\frac{\rho_1 + \rho_2}{2} + \rho_{contaminant}\right) \qquad (10)$$

In the above equation, the term placed outside the parentheses, including the flow stress of the softer material σ_{soft} and the contact normal pressure σ_n, is the ratio of the real contact area to the apparent area obtained by Bowden and Tabor.[21] The bulk electrical resistivities of the materials in contact are ρ_1 and ρ_2, and $\rho_{contaminant}$ is the resistivity stemming from surface contaminants such as oxides, surface films and dirt. The increased resistivity at the contact interfaces results in increased heating by the Joule effect (see $\dot{q}_{electrical}$ in equation (7)).

Numerical implementation

Figure 1 includes a schematic outline of the numerical implementation of the couplings between the previously described finite element modules. As shown in the figure, the coupling between the electrical module and the thermal module is stronger than that with the mechanical module, which is applied at the beginning of each step in order to obtain a velocity field and a stress response of the material for subsequent
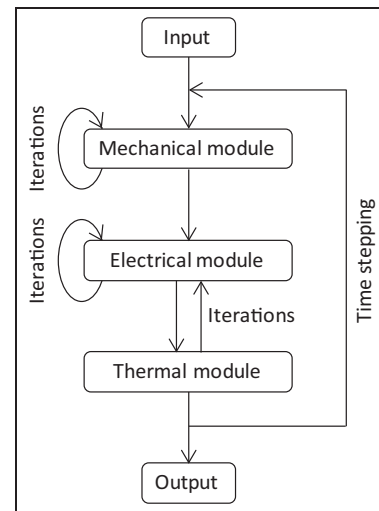

Figure 1. The proposed coupling between the mechanical module, the thermal module and the electrical module of the finite element computer program for resistance welding.

calculations. This is justified by the very small time steps that are needed in order to represent all the physical effects of the welding process. For example, when using AC with a frequency of 50 Hz as the energy source, each half-period has a duration of 10 ms, and proper numerical modelling therefore requires time steps of 1 ms or preferably less. Consequently, instead of having a strong coupling with the mechanical module, as for instance in the case of finite element computer programs for metal forming, the numerical implementation relies on small time steps in a weaker coupling, where the new temperature-dependent material properties are affecting only the mechanical response of the following time step. The corresponding change in the heat generation due to plastic work within a particular step is neglected owing to its insignificant influence compared with that of the electrically generated heat.

The electrical module is applied after the mechanical module in order to supply the thermal module with the current density that is necessary to give rise to heat generation. The electrical module is linear and thus inexpensive to compute when compared with the mechanical model. This is also the main reason why the electrical module and the thermal module are strongly coupled.

Further information on the overall numerical implementation as well as the mechanical, thermal and electrical modules of SORPAS 3D can be found elsewhere.[22]

Modelling conditions and effects under consideration

All the test cases included in this paper make use of two DC06 sheets of 0.8 mm thickness which are welded between two type F1 electrodes with a tip diameter of 6 mm. The sheets are zinc coated with layers 11 μm thick.
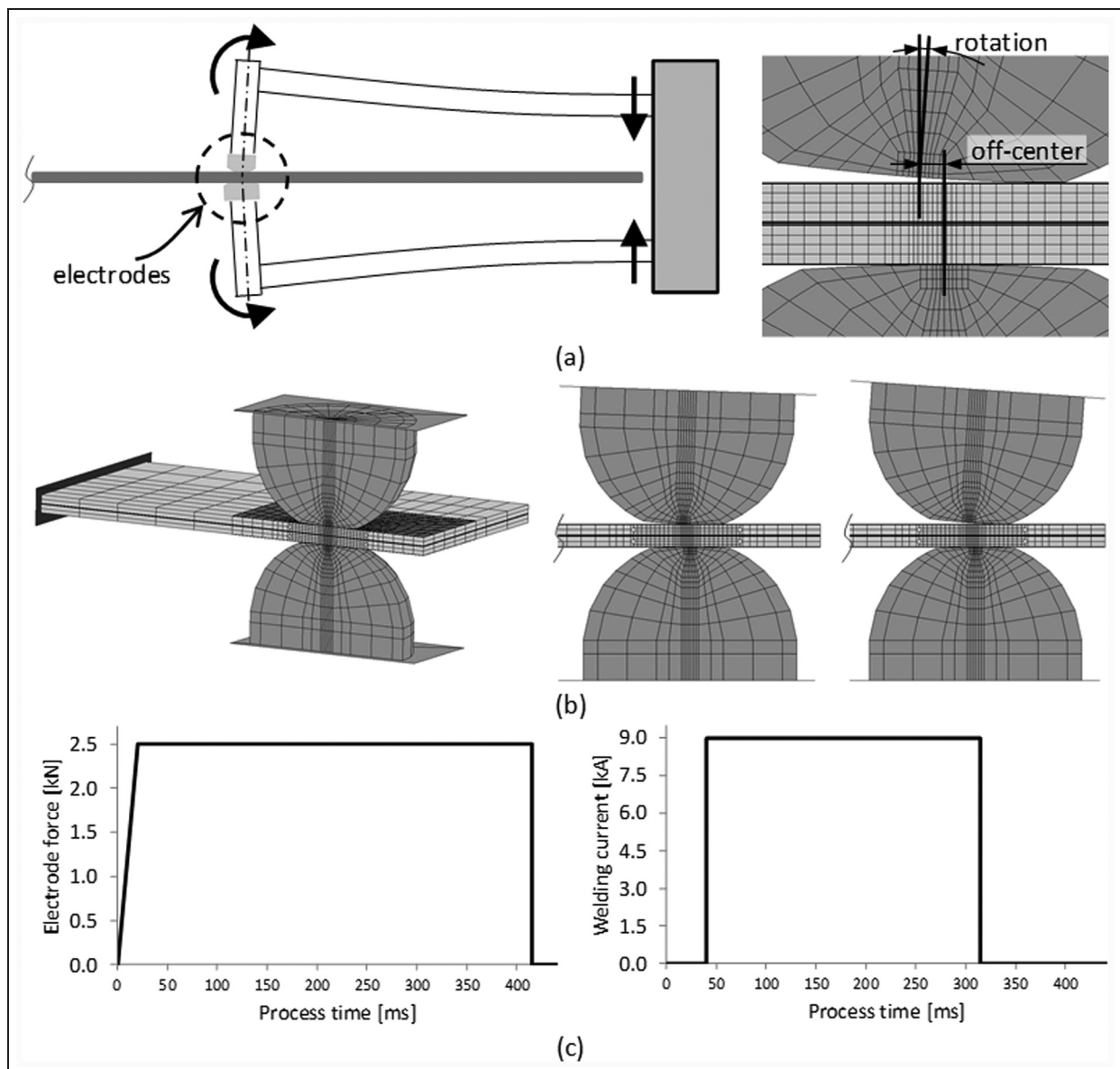
Figure 2. Electrode misalignment and finite element modelling conditions: (a) schematic drawing of the electrode misalignment (left) and identification of the resulting rotation and off-centring of the electrodes (right); (b) discretization of the electrodes and sheets by means of hexahedral meshes, showing the full model with ideally aligned electrodes (left) and 0.5 m relative off-centring and rotations of the upper electrode of 2° and 4° respectively (right); (c) welding parameters in terms of the electrode force and the welding current as functions of the process time.

Electrode misalignment

The flexibility of the welding machine arms for positioning the electrodes and reaching the locations of spots in large sheet panels is a major source of electrode misalignment in resistance spot welding. The problem is schematically illustrated in Figure 2(a), which shows the rotation and off-centring of the electrodes when applying the electrode force through the welding machine arms. Depending on the type of machine and application of force, rotation may occur on one side or on both sides. Relative off-centring may be a result of more rotation on one side than on the other side.

In the case of the numerical simulations performed in this investigation, the discretization of the electrodes

was obtained by uploading their geometry directly from a database of standard electrodes available in the computer program and subsequently performing two clockwise rotations of 2° and 4° in order to replicate the electrode misalignment against the ideal (aligned) perpendicular position between the electrodes and sheets (Figure 2(b)). A relative off-centring of 0.5 mm is also included in the misaligned test cases. The discretization of the sheets was also performed by means of hexahedral elements. The sheets of 40 mm width are clamped 30 mm away from the weld centre and are free on the other end located 10 mm away from the weld centre. The resulting meshes were refined in the region placed in between the electrodes (where the welding nugget
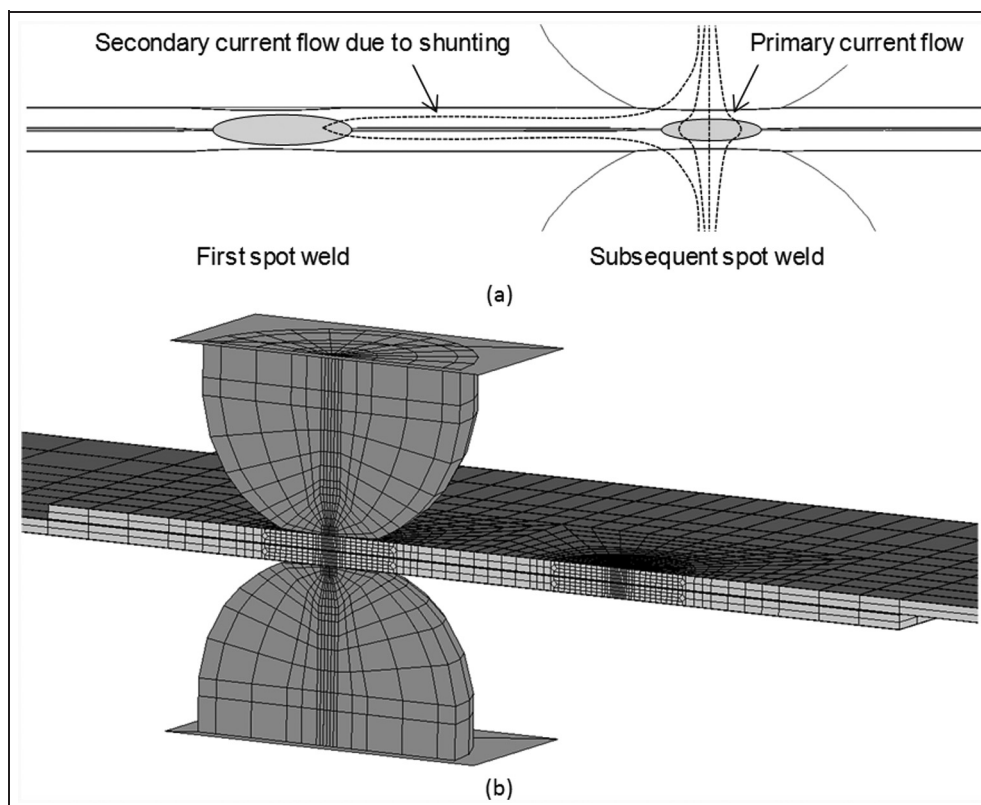
Figure 3. Electrical shunting between consecutive spot welds: (a) schematic drawing of the current being diverted from the intended path because the spot welds are placed close to each other; (b) discretization of the electrodes and sheets by means of hexahedral meshes (the electrodes are positioned according to the first spot weld).

forms and the major deformation takes place). Layers of elements to model the coating and interface conditions were added subsequently by simple mesh extrusion along the sheet surface normals. Only half of the geometry is modelled because of the existence of a vertical symmetry plane. The model consists of a total number of approximately 9000 hexahedral elements.

The choice of hexahedral elements instead of tetrahedral elements, which are the preferential and sometimes only choice in commercial finite element computer programs for metal forming, is justified by the fact that meshes based on tetrahedral elements result in much larger models than alternative meshes based on hexahedral elements for the same level of accuracy. This leads to significant savings in computational requirements and is of critical importance for the computationally intensive electro-thermo-mechanical three-dimensional algorithm illustrated in Figure 1. Moreover, tetrahedral elements are known to cause critical errors when distorted, whereas hexahedral elements behave much better even when distorted.[23] Furthermore, contact is numerically more stable for first-order elements including the utilized hexahedral elements, as opposed to second-order elements that are sometimes applied in tetrahedral meshes to overcome numerical difficulties.

Figure 2(c) shows the welding parameters that are utilized in all cases presented in this paper. The electrode force is constant at a level of 2.5 kN during the welding and hold time. It is numerically raised from zero force during 20 ms. The welding current is constant at 9 kA during the welding time of 275 ms. A hold time of 100 ms, where the electrode force is maintained, was simulated after the end of the welding time.

Shunt effects

Electric shunting between two consecutive spot welds divert the welding current from the intended path and often result in a current density that is not sufficient to produce good-quality spot welds. The phenomenon is schematically illustrated in Figure 3(a). Figure 3(b) shows the hexahedral element discretization of the electrodes and sheets consisting of approximately 16,500 elements. The mesh is again refined at the positions of the two spot welds, which are separated by a distance of 18 mm between their centres. This value is close to, but still above, the recommended minimum distance between spots on 0.8 mm steel sheets.[24] The overall sheet dimensions are 45 mm $\times$ 83 mm. The welding conditions for each weld are identical with those in Figure 2(c). After releasing the force at the end of the hold time of the first spot weld, there is an interval of 2 s before applying the force that is necessary for the second spot weld. Cooling of the first spot weld is simulated during this period.

Mechanical testing

Tensile–shear testing of the sheet combination is also simulated as a continuation of the welding simulation

after cooling to room temperature, removing the electrodes and changing the tool connections (all predefined before starting the computer simulations). Tensile–shear testing is simulated under the same electrode alignment or misalignment as introduced in connection with Figure 2 (i.e. ideal conditions and relative off-centring of 0.5 mm with electrode rotations of 2° and 4° respectively). While the set-up in Figure 2 is associated with corresponding experiments, the tensile–shear testing is only presented by numerical simulations. The sheet dimensions (except for the thickness) are changed and the clamping is removed in order to follow the ISO 14273:2000(E) standard for tensile–shear testing. Each sheet has the dimensions 45 mm × 65 mm (65 mm corresponds to the distance to the clamping tool), and they are placed with an overlap of 35 mm. Figure 4(a) presents the mesh utilized, which consists of approximately 10,000 hexahedral elements, Figure 4(b) presents an example of a simulated weld nugget and initiated cooling, and Figure 4(c) shows the continuation of the tensile–shear testing.

The two sheets welded by two spots in Figure 3 are already prepared as a lap joint which allows subsequent tensile–shear testing. This will be included only to show the possibilities as it would be a similar procedure to test the damage, strength and/or deformation behaviour of a welded structure.

Results and discussion

Electrode misalignment

The simulated weld nuggets for the different electrode alignments are shown in Figure 5, together with a cross-section of the experiment. In the simulations with ideally aligned electrodes in Figure 5(a), the resulting weld nugget is symmetric and the amount of sheet separation is also reasonable and close to symmetric despite the fact that the left side is clamped (30 mm away from the weld centre) while the right side is free (10 mm away from the weld centre). The nugget becomes asymmetric and the electrode indentations in the sheets become severe when the electrodes are misaligned. Figure 5(b) shows the resulting weld when the upper electrode is rotated 2°, and Figure 5(c) shows the resulting weld when the rotation is 4°. The off-centring in both cases is equal to 0.5 mm. The initial contact between the upper electrode and the sheet is only a
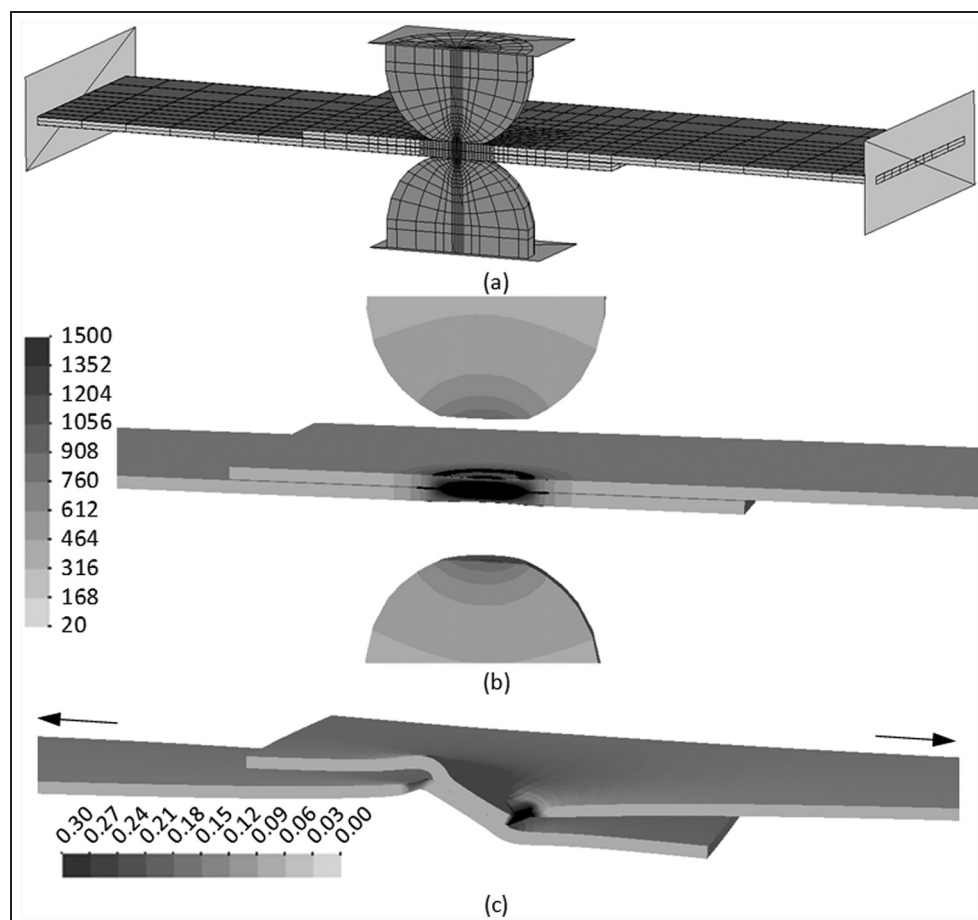

Figure 4. Integrated resistance welding and mechanical testing simulation environment showing (a) the mesh utilized in the numerical modelling, (b) the distribution of the process peak temperature (°C) in the simulated weld nugget after unloading and initiated cooling in air and (c) the subsequent tensile–shear testing with simulated damage according to equation (5). The arrows indicate the loading direction.
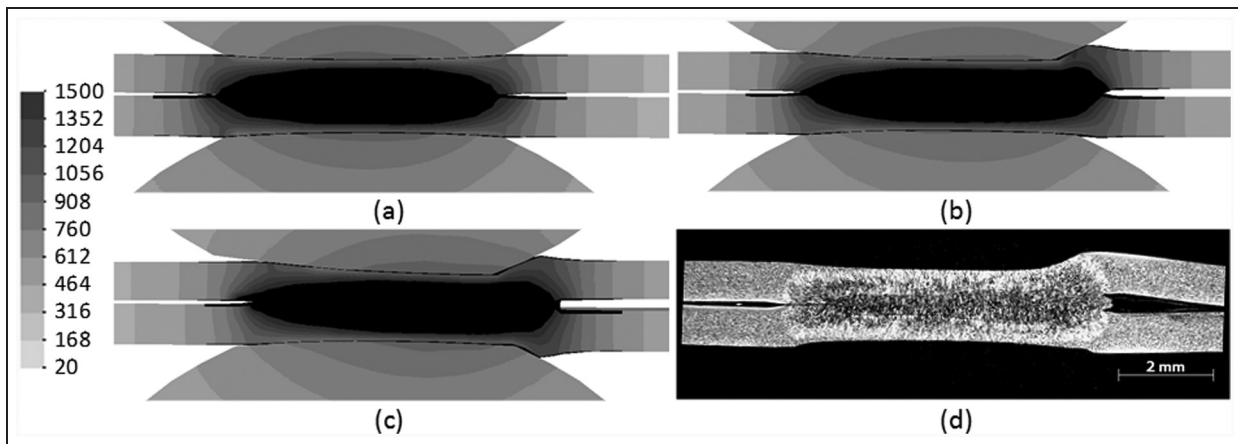
Figure 5. Weld nugget cross-sections obtained from (a)–(c) the finite element predicted geometry and the distribution of the process peak temperature (°C) and (d) the experimental results. The finite element simulations include (a) the ideal electrode alignment and (b), (c) the electrode misalignment by 0.5 mm off-centring and clockwise rotations of the upper electrode of (b) 2° and (c) 4°.

partial ring contact when the electrode is misaligned by rotation. The electrode will indent the sheet in order for the contact area to develop during the process and to carry the applied electrode force. The indentation and separation of the sheets in combination with the asymmetric heat generation result in a high risk of splash, leading to uncontrolled joining conditions. The sheet separation and lifting create problems to the over-all assembly of the sheets in production lines because it gives rise to relative movement of the sheets to a degree that can move them off their positions for subsequent weld spots.

The cross-section in Figure 5(d) shows the experimental weld nugget and the final deformation of the sheets. The experiment was performed with a real welding gun of the same type as in the production line. In this case the electrode misalignment is not fixed during the process, but rather a result of the process. This is in fact the reason for carrying out the simulations because they provide further understanding. The electrodes start close to ideally aligned in the real welding process but, on application of the electrode force, the misalignment develops for the reasons described in connection with Figure 2(a).

The experimental weld in Figure 5(d) compares well with the finite element prediction in Figure 5(b), although it is somewhere in between Figure 5(b) and Figure 5(c). This suggests an effective electrode rotation of the upper electrode of around 2°.

The influence of the electrode misalignment on the weld strength is investigated numerically by performing finite element simulations of the tensile–shear testing as outlined in Figure 4. Following the ISO standard, welding and tensile–shear testing were simulated under the above conditions, including ideally aligned electrodes as well as misaligned electrodes. The three simulated load–elongation curves are shown in Figure 6(a), and Figure 6(b) includes the evolution of the geometry of

the testing specimen at selected points on the curve for the condition without electrode misalignment.

The differences in the load-bearing capacities are surprisingly negligible in the three cases, leading to an immediate conclusion that the electrode misalignment has no influence on the weld strength. This, however, is not confirmed by experiments, and the simulations did not include the eventual splash and the related uncontrolled effects. The results are therefore not presented as a conclusion, but to show the possibilities of simulations when more detailed effects are included.

Figure 6(b) shows the tensile–shear testing procedure by the deformation and damage according to equation (5) at each 1 mm elongation. The load increases with increasing elongation until a maximum weld strength reached at 2.0 mm elongation with a corresponding load of 4.15 kN. This point is reached without severe damage, which accelerates after this point, reducing the load and finally resulting in facture. The region of high damage reveals the location of the onset of fracture (see the region indicated with a circle in Figure 6(b)), and it can therefore be stated from the last figure in Figure 6(b) that the failure type will be thinning and fracture of the sheet, resulting in plug failure. This is the case for all three tensile–shear tests and is typical of sound weld nuggets in thin sheets.

Electrical shunting of welding current

The simulation results of the welding case including the two neighbouring spots introduced in Figure 3 are presented in Figure 7. The figure includes an overview of the simulation procedure and the corresponding temperature development during the overall process. The first welding time finishes after 315 ms, and the finite-element-predicted distribution of the temperature is shown in the upper left figure in Figure 7(a). The electrode force is maintained for an additional 100 ms and
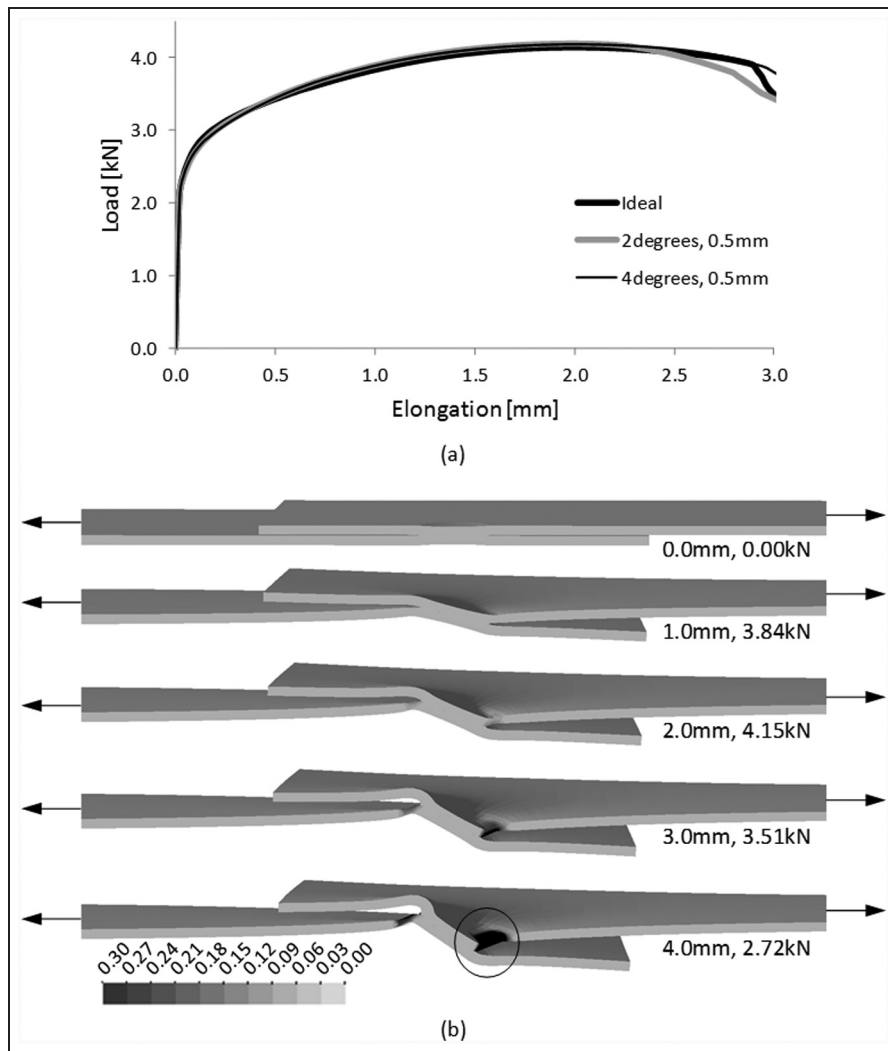
Figure 6. Finite element analysis of tensile–shear testing for different electrode alignments showing (a) the predicted load–elongation curves and (b) the predicted evolution of specimen deformation and damage evolution (equation (5)) for the ideal case.
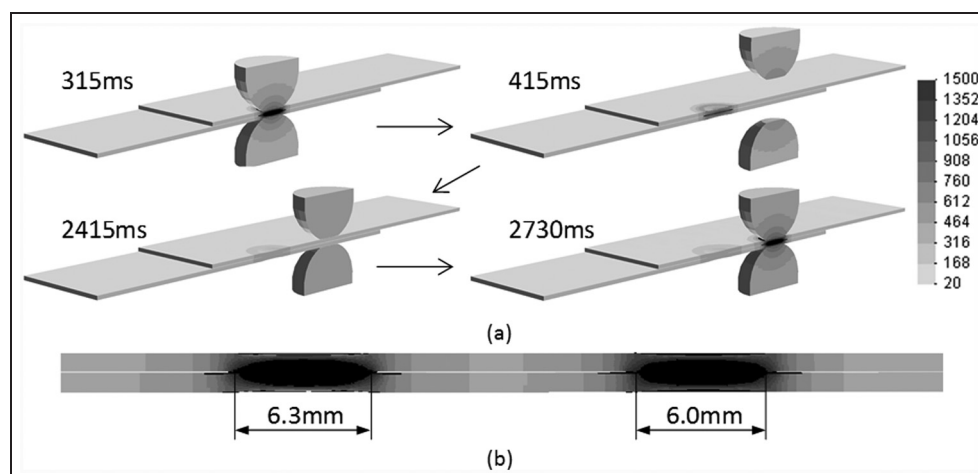

Figure 7. Distribution of the temperature (°C) during numerical simulations of the electric current shunting between two consecutive spot welds shown (a) at different instants of time and (b) in terms of the process peak temperature, revealing the nugget sizes. Both figures share the same colour legend.
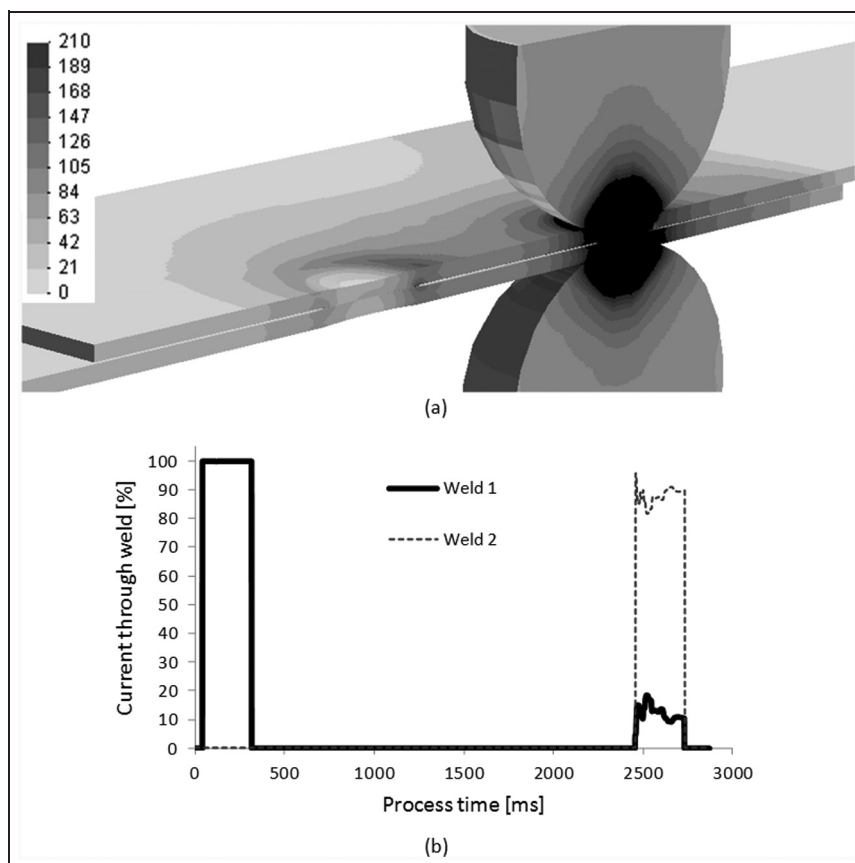
Figure 8. Simulated current flow: (a) predicted current density distribution after 20 ms into the second weld time, where the scale corresponds to 0–210 A/mm^2 out of the maximum 1800 A/mm^2 at this instant of time; (b) current through each of the welding points as a percentage of the total applied welding current.

then moved (instantaneously in the numerical simulations) to the location of the next spot weld. The upper right figure in Figure 7(a) shows the corresponding temperature field, where the weld nugget has solidified. The electrodes are then closed after 2 s, such that the total simulated process time is 2415 ms when starting the second spot weld. The lower left figure in Figure 7(a) includes the corresponding temperature field after the additional cooling time of 2 s. Finally, the lower right figure in Figure 7(a) shows the predicted distribution of temperature after 2730 ms, which corresponds to the end of the second welding time. The second nugget is now in its molten state. The simulations are then completed by an additional hold time of 100 ms and further cooling. At the end of the simulations, the process peak temperature distribution, shown in Figure 7(b), reveals the weld nuggets. The first weld nugget has a predicted diameter of 6.3 mm, while the second weld nugget has a diameter of only 6.0 mm, which is almost 5% smaller than that of the first spot.

The amount of shunting is presented in Figure 8 by the current density distribution at an instant of time and the current through each weld as a function of time. The current density distribution in Figure 8(a) shows how part of the current flows through the sheets and through the previous weld while welding the

second point. In the first spot, the current density is higher around the periphery of the weld owing to the sharp geometrical change. Figure 8(b) shows the percentage of the total current passing through each of the welds as a function of time. The first weld will naturally experience the total welding current. The predicted current through the second weld, following the curve in Figure 8(b), is roughly 90%, while the remaining 10% passes through the first weld because of shunting. The amount of shunting varies during the welding time as a result of the changing contact properties, the material properties and the formation of contact area. From the curve shown in Figure 8(b) it appears that the amount of shunt current initially increases and then decreases towards the end of the welding time. After overcoming the initially high contact resistance, the first increase in the shunt current is explained by the temperature increase in the second weld and the associated increase in the electrical resistivity. The temperature in the first weld and the sheet material in between remains moderate. The subsequent decrease in the amount of shunt current is explained by the increasing contact area, and therefore decreasing resistance, between the sheets where the second weld forms.

Finally, the total strength of the two neighbouring spots is simulated by tensile–shear testing in the length
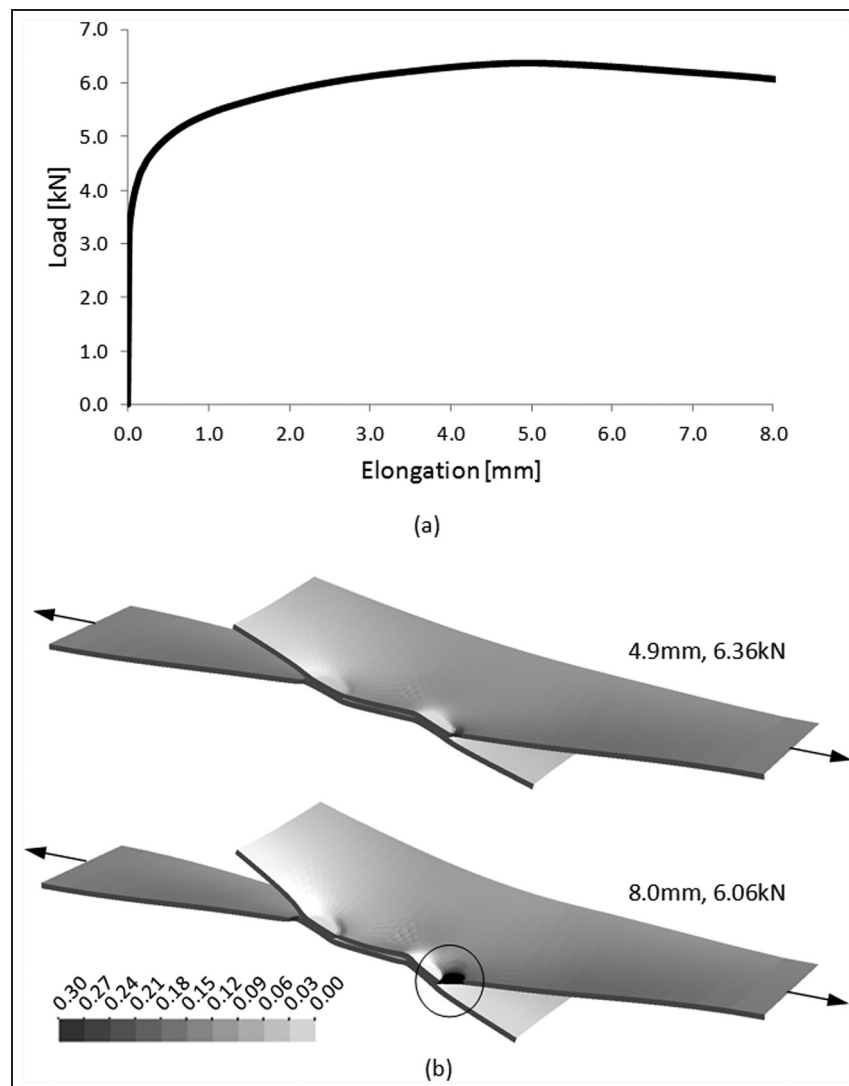
Figure 9. Finite element analysis of the tensile–shear testing of the specimen with two neighbouring spot welds: (a) predicted load–elongation curve; (b) predicted evolution of the specimen configuration during testing including the predicted damage according to equation (5).

direction of the two spots. Figure 9 includes the load–elongation curve as well as the predicted deformation and accumulated damage D at elongations of 4.9 mm and 8.0 mm. The load–elongation curve reveals a maximum load of 6.36 kN at an elongation of 4.9 mm. This testing does not follow any standards, but it illustrates the potential of predicting the strength of a welded structure. The combination of two welds has a higher strength than the single spot does (compare Figure 6(a)) despite the fact that the loading direction sees only one spot. The presence of a neighbouring spot increases the resistance to bending of the sheets near the spots, thereby increasing the strength. Figure 9(b) shows that the first failure is predicted near the second weld (see the region indicated with a circle) as may be expected because of the smaller diameter of the nugget. It also shows that the failure mode is again plug failure.

The decrease in the diameter of the second weld depends on the distance between the spots and may

also be influenced by eventual other previously welded spots. In the simulated case, the current was kept constant to evaluate the effect on the nugget diameter, but it will also be possible to simulate the second weld with an increased welding current to compensate for the shunt effect. An estimate for the new current can thereby be predicted before carrying out further experiments and ultimately production. Simulations can also be utilized in the evaluation of the temperature rise in previous spots, which can reveal whether there is risk of influencing the microstructure formation of previous spots during their cooling. This will depend on the distance and the time between the welds.

Conclusions

Three-dimensional numerical modelling is necessary for obtaining an insight into complex resistance welding

phenomena such as those included in the present paper. Moving from laboratory tests to the production line is all about deviations from ideal conditions and the occurrence of unexpected problems. Therefore, expanding laboratory tests to include the numerical modelling of real production conditions is crucial for increasing the accuracy and reliability of welding operating conditions. The cases presented in this paper for resistance spot welding include some of the more typical challenges which are met in automotive production lines and which may eventually lead to poor welds or ultimately to no joining even though the applied welding schedules work out in ideal laboratory tests.

The modelling conditions that were utilized in this paper replicate the operating conditions of the welding machines which are commonly employed in automotive production lines. In specific terms, the overall flexibility and the resulting electrode misalignment were modelled as closely as possible to real production conditions. The three-dimensional numerical simulations allow visualization of physical effects that are not observed in two-dimensional numerical simulations nor in experimental testing, and it provides the possibility of obtaining a measure of the robustness towards electrode rotation. It was also shown how continuation of the simulations by tensile–shear testing can be successfully utilized to evaluate the strength and failure modes of the created spot welds.

Another complication considered in the paper is the shunt effect between consecutively welded spots close to each other. Again, three-dimensional numerical modelling proves efficient to show how the current flows through a previous spot weld, and to evaluate the amount of shunt current during the welding time. The influence of the shunt effect on the resulting weld nugget sizes is also evaluated. The analysis could be further extended to find the necessary increase in the current during the second weld to obtain a nugget size identical with that of the first nugget. Finally, the specimen containing the two spots was tested in order to demonstrate the overall testing capability of the new proposed simulation environment.

Acknowledgements

Declaration of conflict of interest

The authors declare that there is no conflict of interest.

References

1. Greenwood JA. Temperature in spot welding. *Br Weld J* 1961; 8: 316–322.
2. Nied HA. The finite element modeling of the resistance spot welding process. *Weld J* 1984; 63: 123s–132s.
3. Nishiguchi K and Matsuyama K. Influence of current wave form on nugget formation phenomena when spot welding thin steel sheet. *Weld World* 1987; 25: 222–244.
4. Tsai CL, Jammal OA, Papritan JC and Dickinson DW. Analysis and development of a real time control methodology in resistance spot welding. *Weld J* 1992; 70: 339s–351s.
5. Khan JA, Xu L and Chao Y. Numerical simulation of resistance spot welding process. *Numer Heat Transfer Part A* 2000; 37: 425–446.
6. Zhang W, Hallberg H and Bay N. Finite element modeling of spot welding similar and dissimilar metals. In: *7th international conference on computer technology in welding*, San Francisco, California, USA, 8–11 July 1997, NIST Special Publication 923, pp. 364–373. Gaithersburg, Maryland: NIST.
7. Huh H and Kang WJ. Electrothermal analysis of electric resistance spot welding processes by a 3-D finite element method. *J Mater Processing Technol* 1997; 63: 672–677.
8. Feulvarch E, Robin V and Bergheau JM. Resistance spot welding simulation: a general finite element formulation of electrothermal contact conditions. *J Mater Processing Technol* 2006; 153–154: 436–441.
9. Nielsen CV, Friis KS, Zhang W and Bay N. Three-sheet spot welding of advanced high-strength steels. *Weld J* 2011; 90: 32s–40s.
10. Larsson JK, Lundgren J, Asbjörnsson E and Andersson H. Extensive introduction of ultra high strength steels sets new standards for welding in the body shop. *Weld World* 2009; 53(5–6): 4–14.
11. Aslanlar S, Ogur A, Ozsarac U and Ilhan E. Welding time effect on mechanical properties of automotive sheets in electrical resistance spot welding. *Mater Des* 2008; 29: 1427–1431.
12. Xu F, Sun G, Li G and Li Q. Failure analysis for resistance spot welding in lap-shear specimens. *Int J Mech Sci* 2014; 78: 154–166.
13. Radakovic DJ and Tumuluru M. An evaluation of the cross-tension test of resistance spot welds in high-strength dual-phase steels. *Weld J* 2012; 91: 8s–15s.
14. Lin HL, Chou T and Chou CP. Modelling and optimization of the resistance spot welding process via a Taguchi–neural approach in the automobile industry. *Proc IMechE Part D: J Automobile Engineering* 2008; 222(8): 1385–1393.
15. Ouisse M and Cogan S. Robust design of spot welds in automotive structures: a decision-making methodology. *Mech Systems Signal Processing* 2010; 24: 1172–1190.
16. Shima S and Oyane M. Plasticity theory for porous metals. *Int J Mech Sci* 1976; 18: 285–291.

17. Doraivelu SM, Gegel HL, Gunasekera JS et al. A new yield function for compressible P/M materials. *Int J Mech Sci* 1984; 26: 527–535.

18. Nielsen KL. *Modelling of damage development and ductile failure in welded joints.* PhD Thesis, Technical University of Denmark, Kongens Lyngby, Denmark, 2009.

19. Greenwood JA and Williamson JBP. Electrical conduction in solids II. Theory of temperature-dependent conductors. *Proc R Soc Lond, Ser A, Mathl Phys Sci* 1958; 246: 13–31.

20. Zhang W. Design and implementation of software for resistance welding process simulations. *Trans ASME, J Mater Mfg* 2003; 112: 556–564.

21. Bowden FP and Tabor D. *The fabrication and lubrication of solids*. Oxford: Oxford University Press, 1950.

22. Nielsen CV, Zhang W, Alves LM et al. Modeling of thermo-electro-mechanical manufacturing processes with applications in metal forming and resistance welding. Berlin: Springer, 2012.

23. Kraft P. Automatic remeshing with hexahedral elements: problems, solutions and applications. In: *8th international meshing roundtable*, South Lake Tahoe, California, USA, 10–13 October 1999, pp. 357–367.

24. RWMA. *Resistance welding manual*. Miami, Florida: American Welding Society, 2003.